

MULTIPLE GRAVITY ASSISTS, CAPTURE, AND ESCAPE IN THE RESTRICTED THREE-BODY PROBLEM

SHANE D. ROSS* AND DANIEL J. SCHEERES†

Dedicated to the memory of Kevin Granata and Liviu Librescu.

Abstract. For low energy spacecraft trajectories such as multi-moon orbiters for the Jupiter system, multiple gravity assists by moons could be used in conjunction with ballistic capture to drastically decrease fuel usage. In this paper, we investigate a special class of multiple gravity assists which can occur outside of the perturbing body's sphere of influence (the Hill sphere) and which is dynamically connected to orbits that get captured by the perturber and orbits which escape to infinity. We proceed by deriving a family of symplectic twist maps to approximate a particle's motion in the planar circular restricted three-body problem. The maps capture well the dynamics of the full equations of motion; the phase space contains a connected chaotic zone where intersections between unstable resonant orbit manifolds provide the template for lanes of fast migration between orbits of different semimajor axes. Within the chaotic zone, the concept of a set of reachable orbits is useful. This set can be considered bounded by, on one end, orbits leading to ballistic capture around the perturber, and on the other end, the orbits escaping to infinity or a bounding surface at finite distance.

Key words. three-body problem, celestial mechanics, symplectic maps, phase space transport

AMS subject classifications. 70F07, 70F15, 37J45, 70H33

1. Introduction. In recent numerical constructions of multi-moon orbiters for the Jupiter system, multiple gravity assists for a spacecraft in the exterior and interior Hill's regions were used to construct low energy transfers between moons [25, 35]. These gravity assists do not lend themselves to the patched-conics approach of astrodynamics as they occur even when the spacecraft remains outside of the perturbing moon's sphere of influence or Hill sphere.

In this paper, we investigate such gravity assists by the explicit construction of an energy kick function approximating the effect of the perturbing moon on a spacecraft's jovian orbit. We use Picard's method of successive approximations to generate a symplectic twist map for the planar restricted three-body problem which approximates a Poincaré map at the surface of section corresponding to the periapsis condition. Other authors [23, 6, 16, 36] have considered similar maps to study the long-time evolution of nearly parabolic comets.

The family of maps we develop are applicable to objects on near-Keplerian elliptical orbits of low, moderate and high eccentricity. We are especially interested in the dynamics of objects whose periapse or apoapse (closest and furthest approach to the central body, respectively) grazes the Hill sphere of the perturbing body. The engineering application envisioned is the design of low energy trajectories [7, 2], specifically between moons in the satellite system of one of the giant planets [15, 12]. Multiple gravity assists in resonance with the perturber are a key physical mechanism which could be exploited in future scientific missions [25]. For example, a trajectory sent from Earth to the Jovian system, just grazing the orbit of the outermost icy moon Callisto, can migrate using little or no fuel from orbits with large apoapses to smaller

*Engineering Science and Mechanics, Virginia Polytechnic Institute and State University, 224 Norris Hall, MC 0219, Blacksburg, VA 24061; E-mail: sdross@vt.edu; tel: (540) 231-1616; fax: (540) 231-4574

†Aerospace Engineering, University of Michigan, 3048 FXB, Ann Arbor, MI 48109-2140, USA; E-mail: scheeres@umich.edu; tel: (734) 615-3282; fax: (734) 763-0578

ones.

The advantage of considering an analytical two-dimensional map as opposed to full numerical integration of the restricted three-body equations of motion is that we can apply all the theoretical and computational machinery applicable to phase space transport in symplectic twist maps [24, 19, 9]. We also make connections with earlier work on the restricted three-body problem, particularly capture via tube dynamics [14]. The result is a fuller picture of the global dynamics in the restricted three-body problem.

The paper is organized as follows. In §2, we write the Hamiltonian for the restricted three-body problem in a form appropriate for application of Picard’s method and introduce the energy regime we are considering. In §3, we apply Picard’s method of successive approximations to determine the orbital changes over one orbit. In §4, we develop a family of area-preserving twist map approximations to the Poincaré return map which take one periapsis passage to another for orbits exterior to the secondary mass. The dynamics of the maps are discussed in §§5 and 6, in particular the relationship of multiple gravity assist trajectories to capture around the secondary mass and escape to infinity. We discuss our results and indicate future directions in §7.

2. The Hamiltonian. Consider the planar circular restricted three-body problem (PCR3BP), with a test particle P in the gravitational field of two primary masses, m_1 and m_2 , which are on circular orbits about their common center of mass. For illustrative purposes, we take m_1 to be Jupiter, m_2 to be one of its moons, and the particle to be a natural object or spacecraft of insignificant mass.

We use the standard system of units; the m_1 - m_2 distance is scaled to 1, as is their mean motion about the center of mass, and their mass ratio is $\mu = m_2/(m_1 + m_2) \ll 1$. The PCR3BP is a perturbation of the two-body Kepler problem, where the particle is assumed to be on a near-Keplerian orbit around the m_1 - m_2 barycenter. We can write the Hamiltonian in a frame centered on the barycenter,

$$(2.1) \quad H_{\text{iner}} = \frac{1}{2}(p_x^2 + p_y^2) - \frac{1-\mu}{r_1} - \frac{\mu}{r_2}.$$

We can write r_1 and r_2 in terms of (r, θ) , where $r \gg \mu$ is the distance between the particle and the barycenter and θ , as shown in Figure 2.1, is the angle between the particle and m_2 , measured from the barycenter. Using $r = \sqrt{r_1^2 - 2\mu r_1 \cos \theta + \mu^2} =$

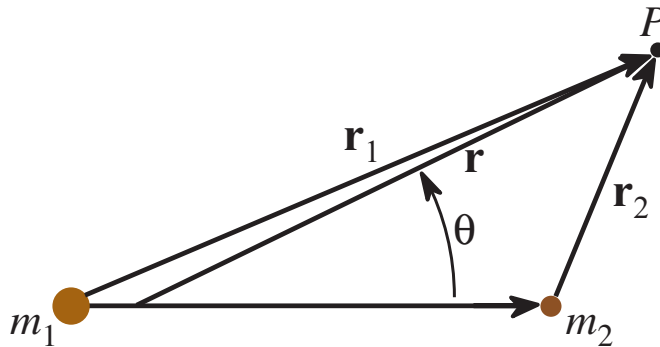


FIG. 2.1. *The relationship between distances in the restricted three-body problem.*

$r_1 - \mu \cos \theta + \mathcal{O}(\mu^2)$ we can write

$$(2.2) \quad \frac{1}{r_1} = \frac{1}{r} - \frac{\mu}{r^2} \cos \theta + \mathcal{O}(\mu^2)$$

Our Hamiltonian (2.1) can be rewritten as

$$(2.3) \quad \begin{aligned} H_{\text{iner}} &= \left(\frac{1}{2}(p_x^2 + p_y^2) - \frac{1}{r} \right) + \mu \left(-\frac{1}{r_2} + \frac{\cos \theta}{r^2} + \frac{1}{r} \right) + \mathcal{O}(\mu^2), \\ &= K + \mu R + \mathcal{O}(\mu^2), \end{aligned}$$

where $K = -1/(2a)$ is the Keplerian part and μR the perturbing part to first order in μ . The particle's phase space position is given by its instantaneous semimajor axis a , eccentricity e , argument of periapsis ω , and true anomaly ν , which have geometric descriptions as given in Figure 2.2. These orbital elements are referred to as ‘‘osculating’’ or instantaneous orbital elements since they represent an instantaneous approximation of the motion of the object as a Keplerian orbit, which is the kind of orbit it would have if other perturbations were not present. In a celestial mechanics perturbation problem like the one we are considering, these elements are very useful.

For the perturbing function, we have

$$(2.4) \quad \begin{aligned} R &= -\frac{1}{r_2} + \frac{\cos \theta}{r^2} + \frac{1}{r}, \\ &= -\frac{1}{\sqrt{1 + r^2 - 2 r \cos \theta}} + \frac{\cos \theta}{r^2} + \frac{1}{r}. \end{aligned}$$

The angle θ can be related to the traditional osculating elliptic elements of the particle as $\theta = \omega + \nu - t$, where $\nu = \nu(t)$ is the true anomaly of the particle and a function of time, ω is the particle's angle of periapsis, $r = p/(1 + e \cos \nu)$ and $p = a(1 - e^2)$.

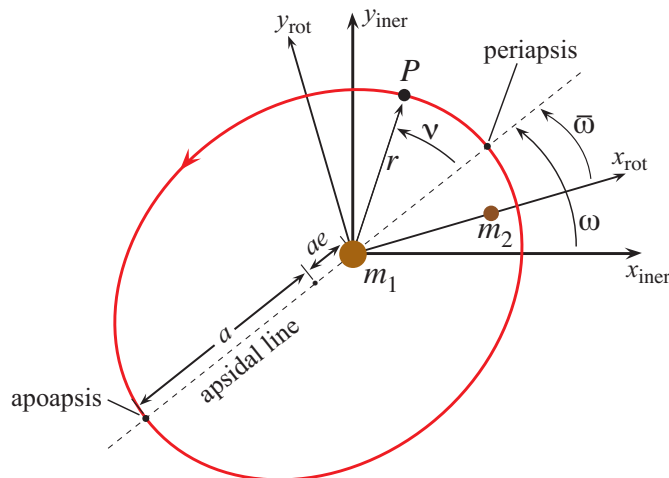


FIG. 2.2. The osculating or instantaneous orbital elements for a particle P in a near-Keplerian orbit about a massive central body m_1 . The perturbing body, m_2 , is in a circular orbit about m_1 of unit frequency and the x axis of the rotating frame is defined as the line from m_1 to m_2 , where the y axis of the rotating frame completes a right-handed coordinate system.

In the frame co-rotating with m_2 and m_1 about their barycenter, the time-dependent Hamiltonian (2.3) can be rewritten in a time-independent form

$$(2.5) \quad H_{\text{rot}}(a, e, \bar{\omega}, \nu) = K(a) + \mu R(a, e, \bar{\omega}, \nu) - G(a, e),$$

where $G = \sqrt{a(1-e^2)} = \sqrt{p}$ is the angular momentum of the particle's orbit and we drop the $\mathcal{O}(\mu^2)$ terms. In the rotating frame, the coordinate conjugate to G is $\bar{\omega} = \omega - t$, the angle of periapsis measured from the m_1 - m_2 line. Hamiltonian (2.5) is time-independent [31] and therefore constant along particle trajectories. We refer to this constant as the Jacobi constant, $C_J = -2H_{\text{rot}}$. Although the invariance of the Hamiltonian in the rotating frame is useful, we continue to use ω (in the inertial frame) for the computations described in the next section.

The Jacobi constant allows us to obtain a coarse partition of accessible phase space for the particle. For some values of C_J , there are inaccessible regions in the rotating frame. The inaccessible regions whose boundaries are zero velocity curves divide the accessible regions, known historically as Hill's regions, naturally into three regions. For a given μ there are five basic cases of connectivity between the regions, corresponding to five intervals of C_J (see [14] for details). The cases are shown in Figure 2.3. The divisions between the cases are given by the Jacobi constant at the Lagrange points, i.e., $C_i = C_J(L_i)$.

We are focusing on particle motion which remains in the exterior region. According to the cases, this would mean $C_J > C_2$. In the Jupiter-Callisto system ($\mu = 5.667 \times 10^{-5}$), for example, we have $C_2 = 3.00618$. Even though motion from the exterior to the regions around m_2 and m_1 are possible for cases 3 and above we find that for energies close to but below C_2 , particle motion can remain in the exterior region for long times. Transit from the exterior region to the region around m_2 is possible for $C_J < C_2$, and the connection between multiple gravity assists and capture orbits will be discussed in §6.

3. Changes in Orbital Elements Over One Orbit. To evaluate changes in the osculating orbital elements over one orbit, we use the first iteration of Picard's method of successive approximations, following [27] and [33].

Picard Iteration. First, we introduce Picard's method. Let $t \in \mathbf{R}$ be the time and $x(t)$ and $f(x, t)$ be functions with values in \mathbf{R}^n . Consider the problem of finding solutions for the following dynamical system,

$$(3.1) \quad \begin{aligned} \frac{dx}{dt} &= f(x, t), \\ x(t_0) &= x_0, \end{aligned}$$

where $t_0 \in \mathbf{R}$ and $x_0 \in \mathbf{R}^n$ are the initial time and configuration of the system.

The Picard iterate of a function $y(t)$ with initial condition x_0 is defined as

$$(3.2) \quad P_{x_0} y(t) = x_0 + \int_{t_0}^t f(y(\tau), \tau) d\tau.$$

Let $P_{x_0}^2 y(t) = P_{x_0}(P_{x_0} y(t))$, $P_{x_0}^3 y(t) = P_{x_0}(P_{x_0}^2 y(t))$, and so on. If f and $\frac{\partial f}{\partial t}$ are continuous, then it can be shown that given any continuous initial curve $y(t)$, its m th Picard iterate $P_{x_0}^m y(t)$ converges to the solution of (3.1) as $m \rightarrow \infty$, if t is in a suitable interval of values close to t_0 (see for example, [4]).

Approximating Changes in Orbital Elements. We use Picard's method as follows. Suppose $y(t)$ represents the osculating orbital elements of a particle in an orbit about the large primary body m_1 . The function f includes the perturbation of the secondary body m_2 of mass μ . The unperturbed orbital elements are a constant function $y(t) = x_0$ over the time interval $[t_0, t_1]$, $t_1 > t_0$. The first iteration of Picard's method yields

$$(3.3) \quad P_{x_0}y(t) = x_0 + \int_{t_0}^t f(x_0, \tau) d\tau,$$

where the time variation in the integrand is due to the perturbation of the m_2 and the true anomaly ν of the particle orbit. Noting that $P_{x_0}y(t_0) = x_0$, and making the approximation $y(t_1) \approx P_{x_0}y(t_1)$, we derive the first order change in the orbital elements over one orbit as

$$(3.4) \quad \Delta y = \int_{t_0}^{t_1} f(x_0, \tau) d\tau,$$

where $T = t_1 - t_0$ is one period of the unperturbed particle orbit.

Perturbations to Particles Exterior to the Orbit of the Secondary. Consider a particle in the exterior realm, with Jacobi constant close to but above that of L_2 ;

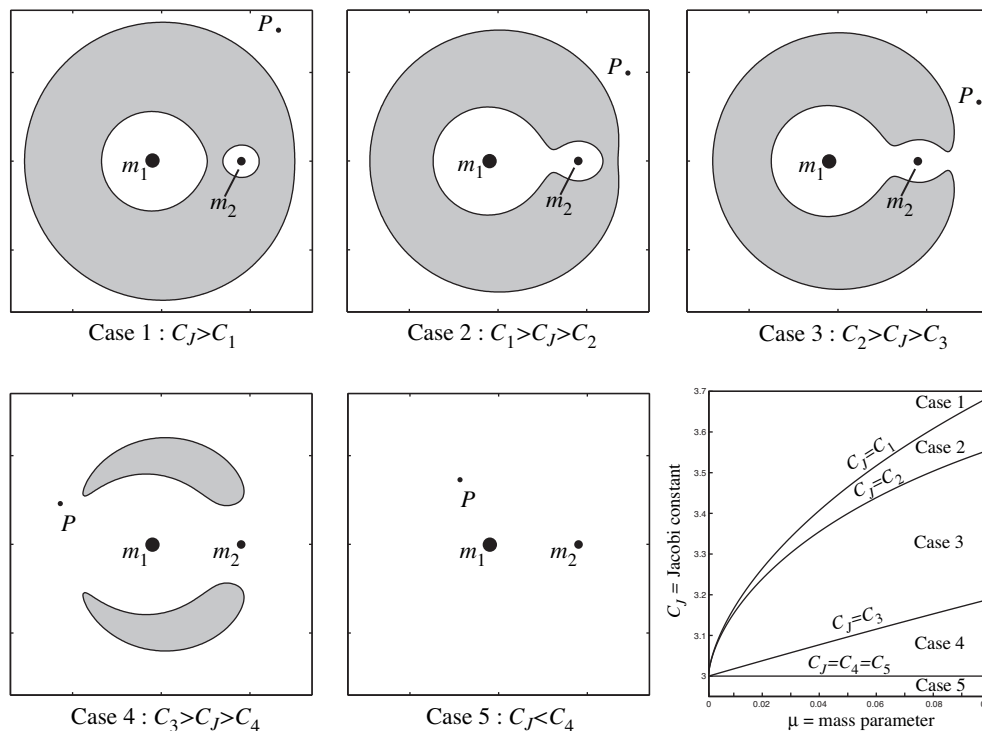


FIG. 2.3. *Regions of possible motion.* Zero velocity curves for five values of the Jacobi constant C_J , one in each of the cases, are shown on the x - y plane for $\mu = 0.3$. These curves bound the zone, in white, accessible by the particle P for a given C_J . The part of the x - y plane which is shaded is inaccessible for a given energy and known as the forbidden region. The outermost accessible exterior region known as the, extends to infinity. In the fifth case, the forbidden region vanishes and motion over the entire x - y plane is possible. In the last panel, the (μ, C_J) -plane is partitioned into the five cases of Hill's regions.

case 2 in Figure 2.3. In this situation, the particle travels on a near-Keplerian orbit around the central mass m_1 . The greatest perturbation occurs at periapsis, when the particle's orbit comes closest to the orbit of the perturbing mass. We therefore take the limits of integration to be from apoapsis to apoapsis, with $t_0 = t_* - T/2$, $t_1 = t_* + T/2$, where $T = 2\pi a^{3/2}$ is the unperturbed orbital period of the particle and t_* is the time of periapsis passage. We take $t_* = 0$ in general. Periapsis passage occurs at $\nu = t = 0$, and thus at the moment over which the perturbation is evaluated, the angles ω , $\bar{\omega}$, and θ coincide.

For our computations, it is useful to use the canonical form of the Lagrange planetary equations [5], which express the change in G as

$$(3.5) \quad \frac{dG}{dt} = -\mu \frac{\partial R}{\partial \omega},$$

where, from (2.4), we calculate

$$(3.6) \quad \frac{\partial R}{\partial \omega} = \frac{r}{r_2^3} \sin(\omega + \nu - t) - \frac{1}{r^2} \sin(\omega + \nu - t).$$

The change in G over one orbit can be computed to first order in μ using (3.5) as the dynamical system for which we apply the approximation (3.4):

$$\begin{aligned} \Delta G &= -\mu \int_{-T/2}^{T/2} \frac{\partial R}{\partial \omega} dt \\ &= -\mu \int_{-T/2}^{T/2} \left[\frac{r}{r_2^3} \sin(\omega + \nu(t) - t) - \frac{1}{r^2} \sin(\omega + \nu(t) - t) \right] dt \\ &= -\frac{\mu}{\sqrt{p}} \int_{-\pi}^{\pi} \left[\left(\frac{r}{r_2} \right)^3 \sin(\omega + \nu - t(\nu)) - \sin(\omega + \nu - t(\nu)) \right] d\nu \\ (3.7) &= -\frac{\mu}{\sqrt{p}} \left[\left(\int_{-\pi}^{\pi} \left(\frac{r}{r_2} \right)^3 \sin(\omega + \nu - t(\nu)) d\nu \right) - \sin \omega \left(2 \int_0^{\pi} \cos(\nu - t(\nu)) d\nu \right) \right]. \end{aligned}$$

If the first integral is expanded as a Fourier series in ω , the integrals can be expressed as functions of Hansen coefficients [28]. However, there is no significant advantage in this for the current application so the integrals are evaluated by quadratures in their current form.

Our goal is to compute ΔK , the change in Keplerian energy over one orbit. By the invariance of the Jacobi constant we have $\Delta H_{\text{rot}} = 0$ and therefore from (2.5):

$$(3.8) \quad \Delta K = \Delta G - \mu \Delta R,$$

where

$$(3.9) \quad \begin{aligned} \Delta R &= R(\nu = \pi) - R(\nu = -\pi), \\ &= \frac{1}{\sqrt{1 + Q^2 + 2Q \cos(\omega + \tau)}} - \frac{1}{\sqrt{1 + Q^2 + 2Q \cos(\omega - \tau)}} + \frac{2}{Q^2} \sin \omega \sin \tau, \end{aligned}$$

with $Q = a(1 + e)$ and $\tau = \pi a^{3/2}$, the apoapsis distance and half period of the unperturbed orbit, respectively.

ΔK is a function of ω , K , and e . The invariance of the Jacobi constant yields a relationship between these three variables, implying $\Delta K = \Delta K_{C_J}(\omega, K)$, where C_J

is a parameter. The expression (3.8) can be written as $\Delta K_{C_J} = \mu f(\omega, K)$, where f is the *energy kick function* following the terminology of [16], [36], and [21]. Physically, the energy kick ΔK_{C_J} between consecutive apoapsis passages can be approximated as a discrete event occurring at periapsis passage. Since $\omega = \bar{\omega}$ at the moment the kick takes place, we will drop the bar from now on, but will consider ω to be the angle of periapsis as measured in the rotating frame, that is, with respect to the m_1 - m_2 line; in other words, ω is the azimuthal separation of the particle and the perturbing body m_2 at the moment of periapsis passage and therefore the moment of the kick.

For our application $Q \gg q > 1$ and it is straightforward to show that ΔR is bounded,

$$(3.10) \quad |\Delta R| \leq \frac{4(Q^2 - \frac{1}{2})}{Q^2(Q^2 - 1)} \approx \frac{4}{Q^2}.$$

For values of K and C_J used in this study, the maximum contribution of $\mu\Delta R$ is much smaller than that of ΔG , so we ignore it for the remainder of the paper, i.e.,

$$(3.11) \quad f(\omega, K) = \Delta K_{C_J}(\omega, K)/\mu = \Delta G/\mu,$$

is assumed.

In Figure 3.1(a), we plot f vs. ω for $C_J = 3$ and an example value of semimajor axis a . Notice that the location and angular width of the greatest perturbations are anti-symmetric about the m_1 - m_2 line ($\omega = 0$) and are independent of the size of the perturbation μ . As shown in Figure 3.1(c), particle orbits whose periapsis passages occur slightly ahead of m_2 in its orbit ($\omega > 0$) will decrease their energy, while those with periapsis passages just behind m_2 ($\omega < 0$) will increase their energy. The location and magnitude of the maximum kicks are plotted as a function of a in Figure 3.1(b).

We want to look at the cumulative effect of multiple passes near m_2 . Such a trajectory has an invariant Jacobi constant, although its orbital elements a and e may change dramatically over time. In the next section, we consider ΔK_{C_J} where $C_J = \text{constant}$. As the orbital energy K and thus the semimajor axis a changes according to ΔK_{C_J} for each kick, e changes to leave invariant (2.5), rewritten as

$$(3.12) \quad C_J = \frac{1}{a} + 2\sqrt{a(1 - e^2)} + 2\mu \left(\frac{1}{r_2} - \frac{1}{r_1} \right).$$

For our application, the terms of $\mathcal{O}(\mu)$ are small and we are left with the Tisserand parameter from which we obtain the eccentricity.

4. The Keplerian Map Derived. Consider the PCR3BP energy surface given by the pair (μ, C_J) , where $\mu \ll 1$ and $C_J \approx 3$ is close to the Jacobi constant of L_2 . We want to compute the sequence of pairs (ω_n, K_n) , $n = 1, 2, 3, \dots$ which result from an initial condition (ω_0, K_0) . These pairs are the azimuthal separation of the particle and the perturbing mass and the particle's Keplerian energy at the n^{th} periapsis passage.

In our approximation, (ω_n, K_n) represents the particle's orbit just before receiving an energy kick. Consider, for example, one of the trajectories in Figure 3.1(c) before the kick was received. Immediately following the kick, the orbit becomes (ω_{n+1}, K_{n+1}) . The time until the next periapsis passage is now $\Delta t = 2\pi a_{n+1}^{3/2} = 2\pi(-2K_{n+1})^{-3/2}$. The change in the periapsis angle during this period is $\Delta\omega = -\Delta t$ modulo 2π . Note, we are neglecting the direct effect of the gravity interaction on the

argument of periapsis, considering only its indirect effect through the change in Keplerian energy. We therefore obtain a two-dimensional update map $(\omega_{n+1}, K_{n+1}) =$

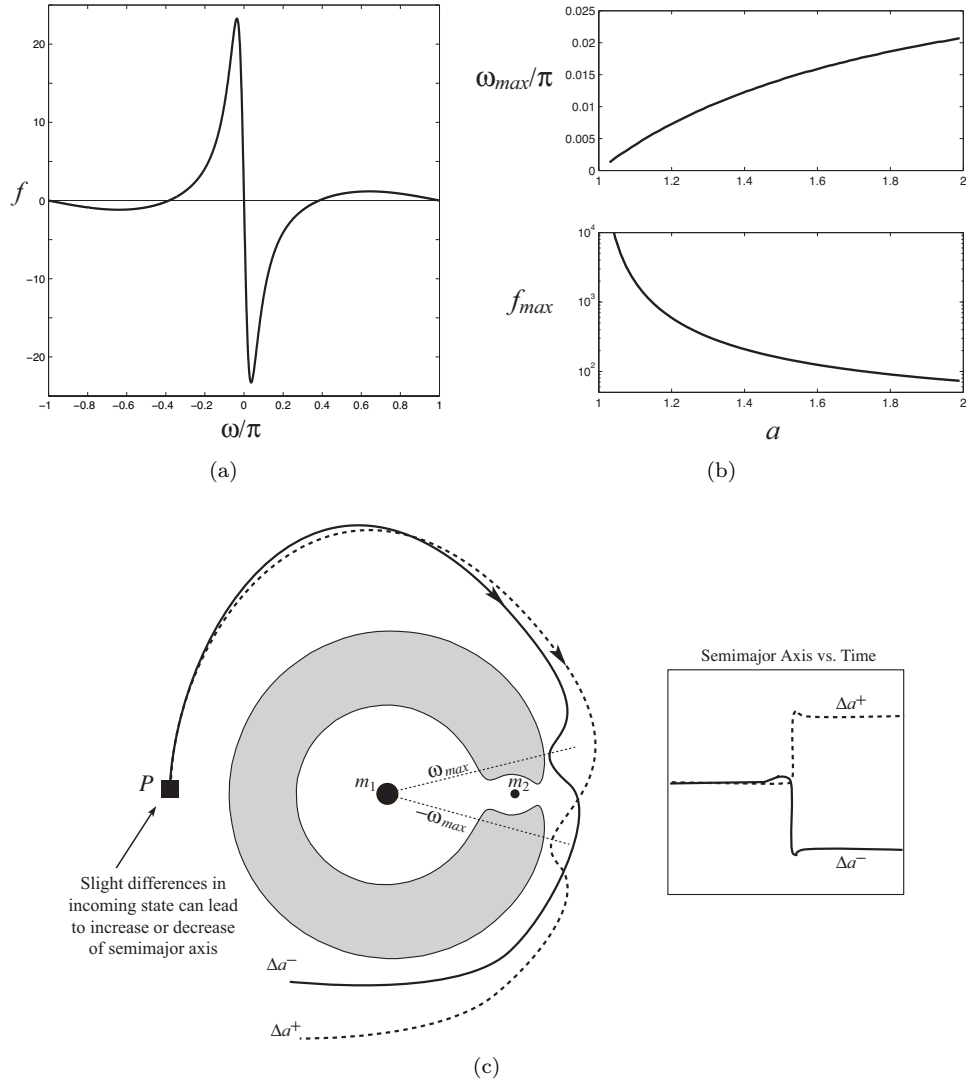


FIG. 3.1. (a) The energy kick function f vs. ω for $C_J = 3$ for $a = 15$. The plot is odd in ω , $f(-\omega) = -f(\omega)$. (b) The location and magnitude of the maximum kicks as a function of a . For f_{max} , the vertical axis is logarithmic. The largest positive kick at $-\omega_{max}$, i.e., $f_{max} = f(-\omega_{max})$. The largest negative kick at ω_{max} with value $-f_{max}$. Notice that smaller a orbits yield larger maximum kicks. (c) Two trajectories with semimajor axis a^0 begin at the same position with slightly different velocities, shown here schematically in the rotating frame for energy case 3. The solid trajectory has its periapsis passage at ω_{max} , receives the largest negative energy kick and drops in semimajor axis, shown in the time history on the right panel. The dashed trajectory has its periapsis passage at $-\omega_{max}$ and gets kicked to a larger semimajor axis. As shown schematically in the time history, the energy kick is nearly instantaneous.

$F(\omega_n, K_n)$ of the cylinder $\mathcal{A} = S^1 \times \mathbf{R}$ onto itself, i.e., $F : \mathcal{A} \rightarrow \mathcal{A}$ where

$$(4.1) \quad F \begin{pmatrix} \omega_n \\ K_n \end{pmatrix} = \begin{pmatrix} \omega_{n+1} \\ K_{n+1} \end{pmatrix} = \begin{pmatrix} \omega_n - 2\pi(-2K_{n+1})^{-3/2} \pmod{2\pi} \\ K_n + \mu f(\omega_n, K_n) \end{pmatrix}.$$

The Jacobian determinant of F is $1 + \mu \frac{\partial f}{\partial K}$. If we assume f is independent of K then we have a symplectic (area-preserving) twist map, desirable for many known properties of such maps [19, 8]. For the remainder of this paper, we neglect the K dependence of f . Given a reference \bar{K} , we let $f(\omega) = f(\omega, \bar{K})$ and thereby make F area-preserving:

$$(4.2) \quad F \begin{pmatrix} \omega_n \\ K_n \end{pmatrix} = \begin{pmatrix} \omega_{n+1} \\ K_{n+1} \end{pmatrix} = \begin{pmatrix} \omega_n - 2\pi(-2K_{n+1})^{-3/2} \pmod{2\pi} \\ K_n + \mu f(\omega_n) \end{pmatrix}.$$

This map has twist to the right,

$$(4.3) \quad \left. \frac{\partial \omega_{n+1}}{\partial K_n} \right|_{\omega_n} = 3\pi (-2(K_n + \mu f(\omega_n)))^{-5/2} > 0,$$

for $K_n < -\mu f(\omega_n)$. From here on, we will understand F to be defined over the appropriate section of the cylinder \mathcal{A} for which (4.3) holds.

The map (4.2) has been called the *Keplerian map* by earlier authors who derived it by other means for the case of near-parabolic orbits [23, 16]. Ref. [21] considered the large a limit, referring to their map as the *eccentric mapping*. Our form is appropriate for elliptical orbits ($e < 1$), even those of low to moderate eccentricity. For a given Jacobi constant and reference energy \bar{K} (where, say, $\bar{K} = K_0$), F is a mapping approximating the dynamics of the PCR3BP for orbits with nearby Keplerian energies, i.e., K_n close to \bar{K} . Specifically, F approximates the Poincaré return map of the fully integrated equations of motion where the surface of section is taken at periapsis, a map used recently in the study of the Hill problem [34, 22].

5. Dynamics of the Keplerian Map. Other authors have considered similar maps to study the long-time evolution of nearly parabolic comets [6, 16, 36]. We apply our map to the identification of transfer trajectories applicable to spacecraft in a planet-moon system. For example, we can consider a spacecraft in the Jupiter-Callisto system ($\mu = 5.667 \times 10^{-5}$) with $C_J = 3$. Using semimajor axis as our vertical coordinate and applying the map (4.2) for several initial values in the (ω, a) -plane results in the left hand plot of Figure 5.1. Throughout the paper we will refer interchangeably between a and K ; the context should make it clear which coordinate we are using.

For our map computations, we need only calculate $f(\omega)$ once from (3.11) for a grid of points $\omega \in [-\pi, \pi]$. Saving the results in a look-up table, we use interpolation to obtain f for arbitrary ω . The initial values for the left hand side of Figure 5.1 were chosen in a connected chaotic sea (an irregular component in the sense of Birkhoff), avoiding the stable islands corresponding to stable mean motion resonances of the particle's orbit with Callisto's. As our phase space is the cylinder, the left and right sides of plot ($\omega = \pm\pi$) are to be identified. The right hand plot shows trajectories computed via full integration of the PCR3BP, using a Poincaré surface of section at periapsis.

The accuracy of the Keplerian map is demonstrated by the resemblance between the results of the map and fully integrated trajectories of the PCR3BP. The location

and widths of the resonant islands appear to be in agreement. As discussed below, the geometrical features directing the motion of phase space regions are approximated well. The notable difference is the “warping” of trajectories of the map near $\omega = 0$, not seen in the full system. The full system Hamiltonian has a discrete time-reversal symmetry such that if (ω_0, a_0) maps to (ω_1, a_1) then $(-\omega_1, a_1)$ maps to $(-\omega_0, a_0)$. In our approximate map this symmetry is broken, albeit slightly.

Some remarks on the resonant structure of the map are in order. Transport in the map can be understood in terms of lobe dynamics and resonance zones [10, 25]. Lobes are parcels of phase space bounded by pieces of stable and unstable manifolds of hyperbolic points. The hyperbolic points of (4.2) occur at $s : r$ mean motion resonances, $a_{res} = (r/s)^{2/3}$, where in inertial space the moon orbits Jupiter r complete circuits for every s particle orbits. In Figure 5.1, these appear as periodic points of period $r - s > 0$. These resonances are also known as being of order $r - s$. For every a_{res} , there is a band of at least $2(r - s)$ alternating elliptic and hyperbolic points, with stable islands (the holes in Figure 5.1) surrounding the elliptic points.

Let’s consider the lowest order resonance in Figure 5.1, the first order 1:2 resonance. The period-one hyperbolic point (fixed point) corresponding to this resonance is located at $p_{res} = (\omega_{res}, a_{res})$, where $\omega_{res} = 0$ and $a_{res} = (2)^{2/3} \approx 1.587$. The stable and unstable manifolds for the hyperbolic point are shown in Figure 5.2. The shaded region is the resonance zone for this resonance, bounded by pieces of upper and lower branches of the stable and unstable manifolds, from the point p_{res} to a primary intersection point of the manifolds. The primary intersection points are also homoclinic orbits doubly asymptotic to p_{res} .

The unstable manifold is produced by first finding the unstable direction in the neighborhood of p_{res} and mapping forward a small seed of points along this direction using F . Linearizing F in the neighborhood of p_{res} , we obtain

$$(5.1) \quad \begin{pmatrix} \delta\omega_{n+1} \\ \delta K_{n+1} \end{pmatrix} = \begin{pmatrix} 1 + \mu\beta\gamma & -\gamma \\ -\mu\beta & 1 \end{pmatrix} \begin{pmatrix} \delta\omega_n \\ \delta K_n \end{pmatrix},$$

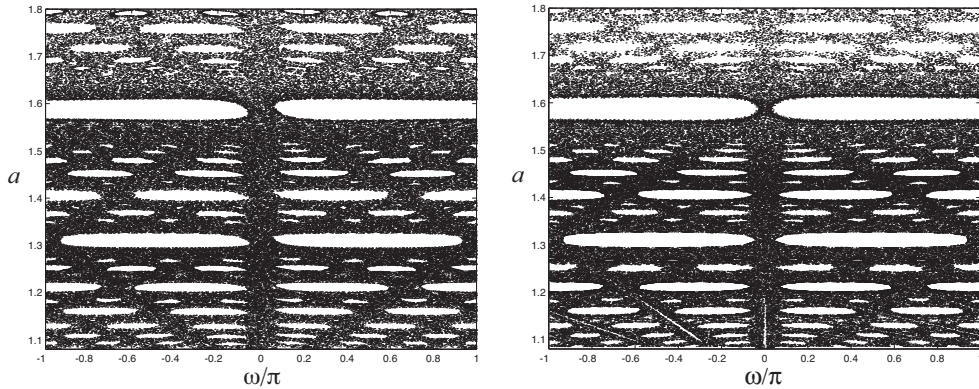


FIG. 5.1. Plot of a vs. ω for $\mu = 5.667 \times 10^{-5}$, $C_J = 3$, $\bar{a} = -1/(2\bar{K}) = 1.35$. The left hand plot shows trajectories computed using the Keplerian map. The right hand plot shows trajectories computed via full integration of the circular restricted three-body problem, using a Poincaré surface of section at periaapsis. The initial conditions for both were taken initially in the chaotic sea and followed for 10^4 iterates, thus producing the ‘swiss cheese’ appearance where holes corresponding to stable resonant islands reside.

where $\beta = -\frac{\partial f}{\partial \omega}|_{\omega=\omega_{res}}$ and $\gamma = 6\pi(a_{res})^{5/2}$. The unstable manifold is locally tangent to the eigenvector belonging to the maximum eigenvalue,

$$(5.2) \quad \lambda = \frac{1}{2} \left(2 + \mu\beta\gamma + \sqrt{\mu\beta\gamma(\mu\beta\gamma + 4)} \right).$$

The stable manifold is produced similarly, substituting F^{-1} for F in the above procedure.

A similar picture of intersecting manifolds exists around each horizontal resonance zone encompassing the stable resonance holes and is similar to the resonance manifolds computed in the full equations [17]. The manifolds of different resonances intersect one another, providing the template for the migration of orbits through semimajor axis.

Finding the Orbits which Yield Maximum Change in Semimajor Axis. We consider the following problem: for a given $a_0 = -1/(2K_0)$, find the ω_0 which yields the maximum change $|a_n - a_0|$ after n periapses. Given our map F , a diffeomorphism of the cylinder to itself, we can consider iterates of the circle at a_0 ,

$$(5.3) \quad \Gamma_0 = \{(\omega_0, a_0) \in \mathcal{A} \mid \omega_0 \in S^1\}.$$

In Figure 5.3(a), we plot Γ_0 and its images $\Gamma_n = F^n(\Gamma_0)$, $n \geq 1$, in terms of the change in semimajor axis $\Delta a = a_n - a_0$ vs. ω_0 . The calculations are for a particle with $a_0 = 1.54$, $C_J = 3$ in the Jupiter-Callisto system, using $\bar{a} = 1.35$ for the map (4.2). The figure shows the effect of multiple periapses, using successive magnifications to reveal the complex self-similar structure as we follow the region with the greatest decrease in semimajor axis.

The function $\Delta a_n(\omega_0)$ gets very complex even for small n . For increasing n , $\max_{\omega_0} \Delta a_n$ and $\min_{\omega_0} \Delta a_n$ have increased magnitude and the domains of the largest changes get thinner. We can estimate the size of these domains as follows. Suppose the local maxima and minima spike features at iterate n have a minimum width $\alpha(n)$ in ω . We can estimate $\alpha(1)$ from the kick function f and then assume $\alpha(n) = [\alpha(1)]^n$. From Figure 3.1, it is reasonable to approximate $\alpha(1)$ as $2\omega_{max}$. For $\bar{a} = 1.35$, we have $\omega_{max} = 0.01\pi$, thus $\alpha(n) = (0.0628)^n$. From simulation, we find that this is

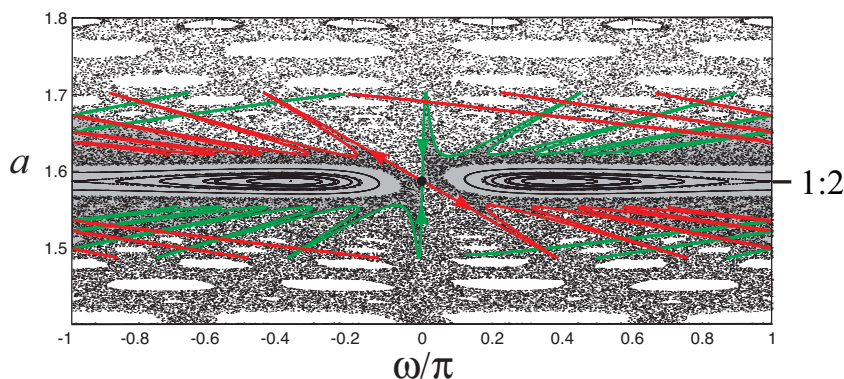


FIG. 5.2. Against the background of Figure 5.1, the stable and unstable manifolds are plotted of the central black point, the period-one hyperbolic fixed point $p_{res} = (\omega_{res}, a_{res}) = (0, (2)^{2/3})$ corresponding to the 1:2 mean motion resonance. The closed curves in the gray region are restricted to the stable island and disconnected from the connected chaotic sea.

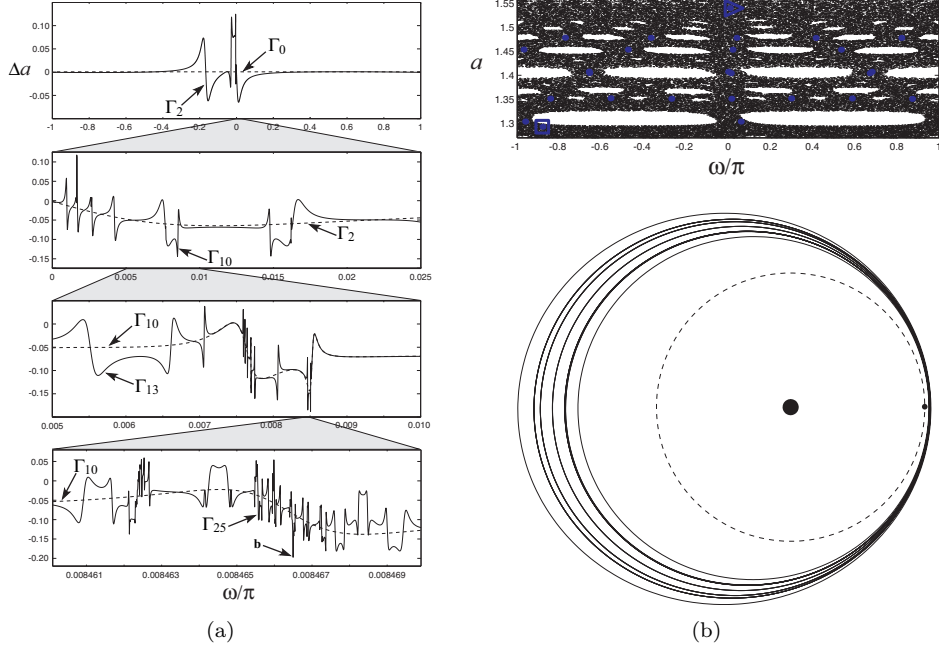


FIG. 5.3. (a) The total change in semimajor axis Δa after n periapsis passages is shown versus the initial angle, ω , where $(\mu, C_J, \bar{a}) = (5.667 \times 10^{-5}, 3, 1.35)$. In the top panel, the initial circle Γ_0 and its second image $\Gamma_2 = F^2(\Gamma_0)$ are shown. The second panel from the top shows a magnification and the tenth image, and so on. The bottom panel shows a portion of ω with Γ_{25} . We see small regions of significantly decreased semimajor axis after 25 periapsis passages. (b) Upper panel: the phase space trajectory of the trajectory marked as **b** in (a). The initial point is marked with a triangle and the final point with a square. Lower panel: the configuration space projections in an inertial frame for this trajectory. Jupiter and Callisto are shown at their initial positions, and Callisto's orbit is dashed. The particle migration is from larger to smaller semimajor axes, keeping the periapsis direction roughly constant in inertial space. Both the particle and Callisto orbit Jupiter in a counter-clockwise sense.

a very conservative lower bound. Nevertheless, for computations to resolve the thin features at iterate n , we use adaptive refinement of a mesh of sample points, described elsewhere [9].

Figure 5.3(b) shows an example of a trajectory which quickly decreases semimajor axis over a duration of 25 orbits. This trajectory corresponds to an initial condition chosen such that it repeatedly experiences a periapsis kick near a minimum of the kick function, Figure 3.1(a). For a randomly chosen initial condition, the effect of such kicks tends to average to zero. But trajectories like the one shown in Figure 5.3(b) can be found which exhibit large increases or decreases over small times, potentially useful trajectories for space missions.

Multiple Gravity Assists Outside Sphere of Influence. We note that over the course of these multiple gravity assists, the particle does not come within the sphere of influence of the perturber. For the example in Figure 5.3(b), the particle at closest approach to the perturber is at a nondimensional distance of $r_{2,min} = 0.0341$, whereas the sphere of influence, approximated as the Hill's radius, is $r_h = (\mu/3)^{1/3} = 0.0266$. The phenomenon involved here is not the typical picture of a gravity assist from the patched-conic perspective, wherein a particle's path enters the sphere of influence of a perturber and can be approximated as a hyperbolic Keplerian trajectory with respect

to the perturber [1].

6. Reachable Orbits, Capture and Escape. Related to the previous discussion is the question of what is the reachable set of orbits as a function of n for orbits initially on the circle Γ_0 ? In Figure 6.1(a), the maximum and minimum semimajor axes reached as a function of the number of orbits are plotted for two values of the Jacobi constant. As particles migrate from an initial semimajor through resonance

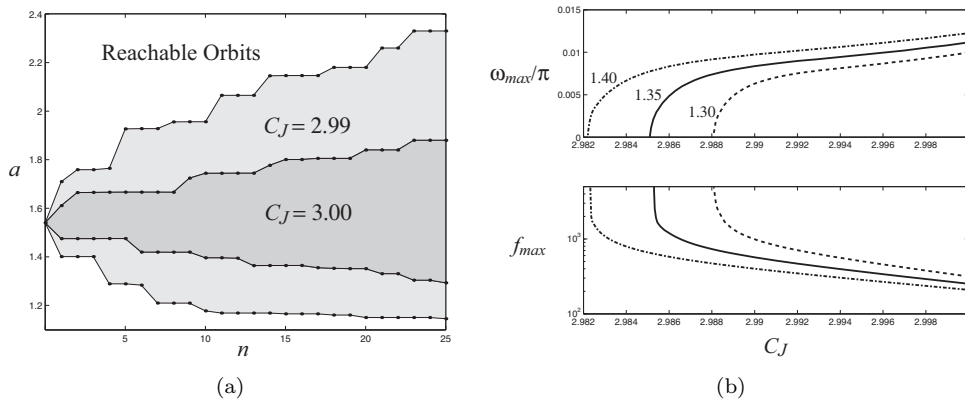


FIG. 6.1. (a) The maximum and minimum semimajor axes reached as function of the number of orbits for a trajectory starting at $a_0 = 1.54$. For $C_J = 3.00$, the reachable orbits are those in the darker shaded zone; for $C_J = 2.99$, the lighter shaded zone. The parameters for the map are the same as in the preceding figures, $\mu = 5.667 \times 10^{-5}$ and $\bar{a} = 1.35$. (b) The variation in the location and magnitude of the maximum kick with Jacobi constant C_J for three values of \bar{a} as labeled (same line labeling for both panels). Values are independent of μ .

zones via lobe dynamics, the set of reachable orbits grows. The maximum (minimum) semimajor axis as a function of n is monotonically increasing (decreasing). Although our map (4.2) lacks the time-reversal symmetry, we can consider it to be close to the time-reversal symmetry of the full PCR3BP equations. In the full equations, the reachable orbit set could be extended to $n < 0$, and would be the mirror image of the $n > 0$ set. This implies that if an orbit of semimajor axis a_n can be reached in n orbits from a_0 , an orbit of semimajor axis $a_{-n} = a_n$ can reach a_0 in n orbits.

For $C_J = 2.99$, the growth is more rapid than for $C_J = 3$. For lower values of Jacobi constant (higher three-body energies, per eq. (2.5)), we expect migration in the phase space to be faster since the kick function yields larger maximum kicks; see Figure 6.1(b).

Variation of ω_{max} and f_{max} with \bar{a} is also shown in Figure 6.1(b). For each \bar{a} , there is a critical value C_J^* corresponding to a periapsis distance of 1 and a singularity of the map. Below C_J^* , the kick function changes its character as the particle can now cross into the interior of the perturber's orbit, a regime investigated by [16].

Exits Leading to Capture. We can consider what the limits to the growth are for the reachable set, in terms of a lower and upper bound in a . We first consider the lower bounds, and consider the full equations of the PCR3BP. For our case of interest, case 3 with $C_J < C_2$, a particle beginning in the exterior realm must remain there for all time in the absence of an outside perturbation (see Figure 2.3); it cannot collide with or enter the phase space realm around m_2 . For C_J below this value, a bottleneck region opens up around the Lagrange point L_2 , permitting particles to enter into orbit around m_2 . In what follows, we summarize the mechanism for this capture as discussed in

detail by [14]. On each three-dimensional energy surface with $C_J < C_2$, within the L_2 bottleneck region there is a planar clockwise orbit surrounding the location of L_2 , shown as a dashed curve in Figure 6.2(a). This orbit has two-dimensional stable and unstable manifolds, with cylindrical ($S^1 \times \mathbf{R}$) geometry. As two-dimensional objects in a three-dimensional energy surface, these cylinders partition the energy surface, acting as separatrices for the flow through the bottleneck region [7, 18]. The interior of these cylinders in the energy surface form three-dimensional tubes of trajectories, termed Conley-McGehee tubes [17]. Only particles inside the tubes will move from the exterior realm to the m_2 realm and vice versa; those outside the tubes will not.

The capture branch of Conley-McGehee tubes associated to the L_2 bottleneck is shown in Figure 6.2(a) as projected onto the configuration space. A tube projection appears as a strip of varying width. Trajectories within the tubes wind around them in phase space and their projection appears similar to the example trajectory within the tube in Figure 6.2(a). There is also an escape branch (not shown) which appears as the mirror image of the capture branch, reflected across the horizontal axis.

In order to find capture trajectories, we consider the Poincaré surface of section taken at periapsis. In terms of the Delaunay (action-angle) variables (L, G, l, ω) where $L = \sqrt{a}$ and l is the mean anomaly, the surface of section at periapsis in the exterior realm is defined as

$$(6.1) \quad \Sigma_e = \{(\omega, a) \in \mathcal{A} \mid l = 0, a > 1\},$$

where the condition of periapsis $l = 0$ is equivalent to setting the true anomaly ν to zero. The Hamiltonian flow induces a Poincaré return map on Σ_e , $\mathcal{F} : \Sigma_e \rightarrow \Sigma_e$ defined for almost all points on Σ_e . In Σ_e , the last cross-section of a tube before it enters the realm around m_2 appears as an exit, diffeomorphic to a disk, as shown schematically in Figure 6.2(b) and numerically in Figure 6.2(c). When trajectories of \mathcal{F} reach the exit, they are transported to the realm around m_2 , where we can consider them emerging within the entrance on Σ_{m_2} , a suitably defined Poincaré surface of section in the m_2 realm.

The Keplerian map F defined in (4.2) is an approximation to \mathcal{F} . When trajectories of F reach the exit, the Keplerian map approximation breaks down and the full equations of motion must be considered. The trajectory can no longer be approximated as near-Keplerian around the central body; it will instead be in orbit about the perturber. We can consider the location of an exit in (ω, a) space (in Σ_e) to give us an effective lower bound in the growth of a reachable set when $C_J < C_2$.

Escaping to Infinity, Upper Bounds and Rotational Invariant Circles. For large values of μ , there may not be an upper bound to the reachable set as n increases. Numerically, we have found some particles which escape onto unbound parabolic and hyperbolic orbits ($K \geq 0$) in finite time ($n < \infty$) from orbits with relatively small a . The set of bound orbits in (ω, K) space which will become unbound after their next periapsis passage is given by lobes bounded above by $K = 0$ and below by $K = -\mu f(\omega)$ when $f(\omega) < 0$ as illustrated in Figure 6.3(a).

If μ is smaller than a critical value, circulating trajectories lying on invariant circles may exist, forming an upper boundary. McGehee [18] proved that for small μ in the PCR3BP, the energy surface is broken up into regions bounded by invariant tori. These invariant tori project onto the darkly shaded annuli A_1 and A_2 shown for case 3 in Figure 6.3(b). These annuli separate the Hill's region into sections corresponding to the invariant regions in the energy surface. For case 3, masses m_1 and m_2 are separated from each other by an invariant torus, thus making it impossible for a

particle to pass from arbitrarily close to m_1 to arbitrarily close to m_2 . Similarly, the two masses are separated from infinity by an invariant torus, i.e., the exterior realm phase space is divided by a transport barrier whose projection onto configuration space is A_2 . Let us call T_2 that part of the exterior realm outside a neighborhood of L_2 which extends up to the bounding surface A_2 .

We find such a boundary in the Keplerian map for small μ values, understood from the point of view of absolute transport barriers in symplectic twist maps of the

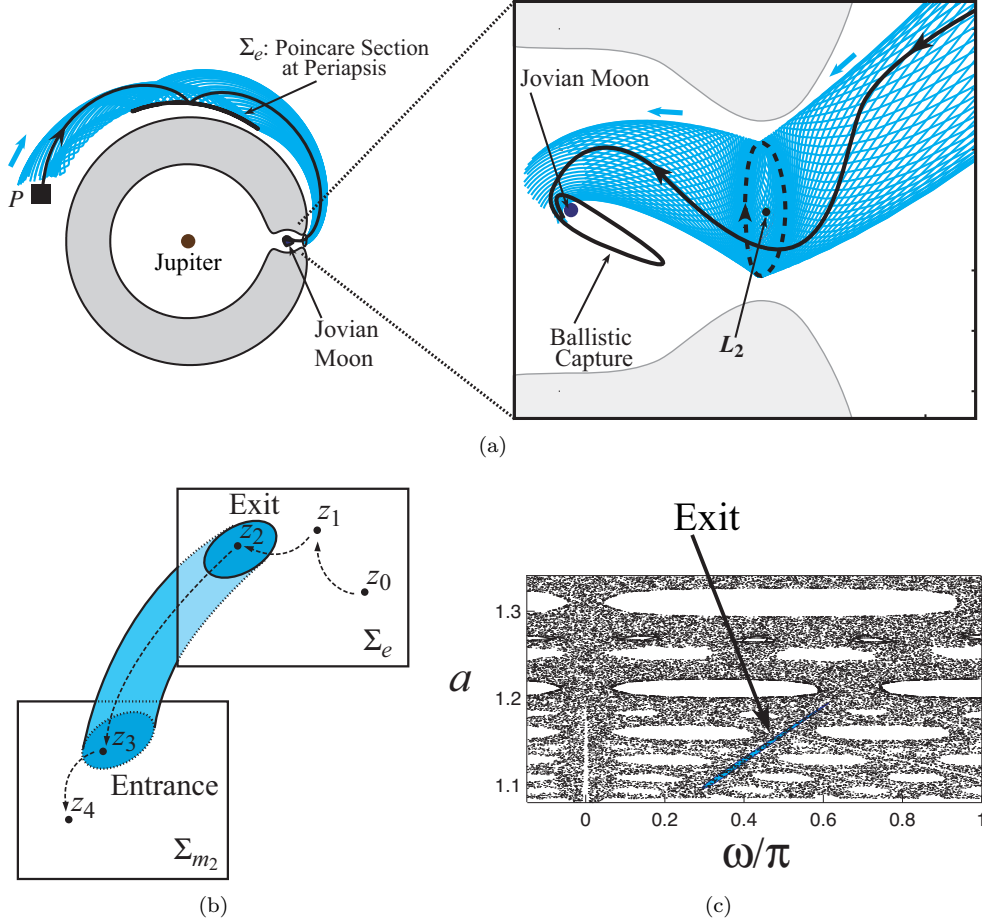


FIG. 6.2. (a) A spacecraft P inside a tube of gravitational capture orbits will find itself going from an orbit about Jupiter to an orbit about a moon, as shown schematically. The spacecraft is initially inside a tube whose boundary is the stable invariant manifold of a periodic orbit about L_2 . The tube, made up of individual trajectories, is shown as projected onto configuration space. (b) Poincaré sections in different realms—in this case in the exterior and m_2 realms, Σ_e and Σ_{m_2} , respectively—are linked by tubes in the phase space which live in surfaces of constant energy ($C_J = \text{constant}$). Under the Poincaré map on Σ_e , a trajectory z_0, z_1, \dots reaches an exit, the cross-section of the tube of capture orbits at the final periapsis before passage through the L_2 bottleneck. Under the Hamiltonian flow, points in the exit of Σ_e map to the entrance of Σ_{m_2} . The trajectory then evolves under the action of the Poincaré map on Σ_{m_2} . (c) The numerically computed location of the exit in configuration space is labeled in the left panel of (a). This surface of section was generated using the full equations of motion with $\mu = 5.667 \times 10^{-5}$ and $C_J = 3.005$.

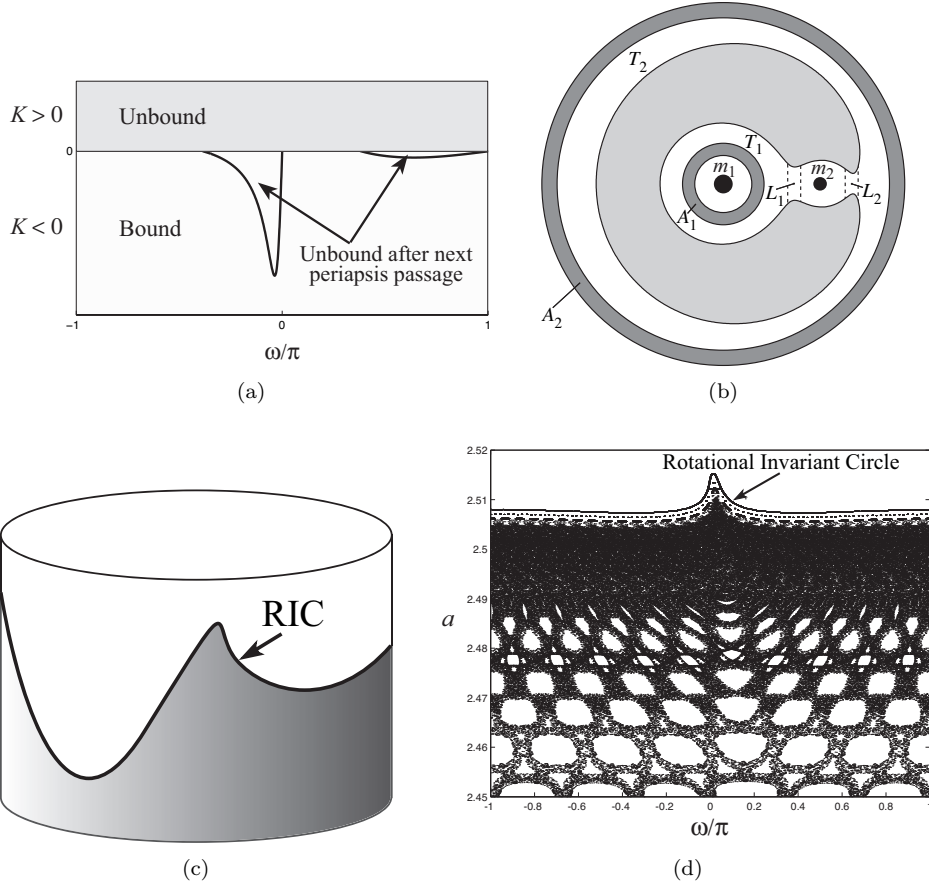


FIG. 6.3. (a) Bound trajectories enclosed by the lobes will become unbound after the next periapsis passage. (b) The projection of invariant tori (darkly shaded) on position space for case 3. (c) A rotational invariant circle (RIC) is an invariant loop that encircles the cylinder, i.e., it cannot be contracted to a point; see Figure 6.3(c). Birkhoff’s theorem [3] implies that any RIC must be the graph of a function, $a = A(\omega)$. An RIC divides the cylinder into two invariant regions. In other words, it prevents transport between the upper and lower “halves” of the cylinder. RICs are in fact the only absolute barriers to transport for symplectic twist maps of the cylinder. Therefore, in connected chaotic sets such as those shown in Figure 5.1 where $a_{min} < a < a_{max}$, we can say that no RIC can exist entirely in that portion of the cylinder. (d) A stable circulating trajectory forms an upper boundary to the chaotic sea preventing particles from migrating to large a values. The calculation was done using the Keplerian map approximation with parameter values $(\mu, C_J, \bar{a}) = (5 \times 10^{-6}, 3, 2.5)$.

cylinder, following [19]. An invariant circle is a curve \mathcal{C} such that $F(\mathcal{C}) = \mathcal{C}$. A rotational invariant circle (RIC) is a closed loop that encircles the cylinder (i.e., it cannot be contracted to a point; see Figure 6.3(c)). Birkhoff’s theorem [3] implies that any RIC must be the graph of a function, $a = A(\omega)$. An RIC divides the cylinder into two invariant regions. In other words, it prevents transport between the upper and lower “halves” of the cylinder. RICs are in fact the only absolute barriers to transport for symplectic twist maps of the cylinder. Therefore, in connected chaotic sets such as those shown in Figure 5.1 where $a_{min} < a < a_{max}$, we can say that no RIC can exist entirely in that portion of the cylinder.

If we find an RIC for our map, we have found an upper bound in the phase space beyond which particles with a greater than but close to 1 cannot pass. As a computational experiment motivated by calculations of [21], we consider the Keplerian map for $(\mu, C_J, \bar{a}) = (5 \times 10^{-6}, 3, 2.8)$. We find an orbit at the top of Figure 6.3(d) which marches around the cylinder, densely covering a circle. This is an RIC at the

lower edge of the 1:4 resonance island and is therefore a bounding surface. By the smoothness of the map F in its parameter μ , we can expect a bounding surface for all μ below at least 5×10^{-6} for fixed C_J and \bar{a} .

This result is based on the structure of symplectic twist maps, and not the KAM theorem [19]. However, we note that in our context the KAM theorem implies that RIC's present in the unperturbed integrable area-preserving map, i.e, (4.2) with $\mu = 0$,

$$(6.2) \quad \begin{pmatrix} \omega' \\ K' \end{pmatrix} = \begin{pmatrix} \omega - 2\pi(-2K)^{-3/2} \pmod{2\pi} \\ K \end{pmatrix},$$

will persist under small area-preserving perturbations of the unperturbed map. For the unperturbed map, all trajectories lie on RIC's. The perturbed map for small μ is written

$$(6.3) \quad \begin{pmatrix} \omega' \\ K' \end{pmatrix} = \begin{pmatrix} \omega - 2\pi(-2K)^{-3/2} - \mu g(\omega, K) \pmod{2\pi} \\ K + \mu f(\omega) \end{pmatrix},$$

where $g(\omega, K) = 6\pi f(\omega)(-2K)^{-5/2}$. In order for there to be invariant circles, we need the average of $f(\omega)$ over ω to be zero,

$$(6.4) \quad \int_{-\pi}^{\pi} f(\omega) d\omega = 0,$$

which our kick function satisfies, being odd in ω . The KAM theorem for our problem takes the form of [20] which says that for sufficiently small perturbations, most RICs will persist.

7. Discussion and Conclusions. Using Picard's method of successive approximations, we derive a family of two-dimensional symplectic twist maps to approximate a particle's motion in the planar circular restricted three-body problem with Jacobi constant near 3. The maps model a particle on a near-Keplerian orbit about a central body of unit mass, where the spacecraft is perturbed by a smaller body of mass μ . The interaction of the particle with the perturber is modeled as an impulsive kick at periapsis passage, encapsulated in a kick function f . The maps are identified as an approximation of a Poincaré return map of the full equations of motion where the surface of section is taken at periapsis, mapping each periapsis passage to the next in terms of ω , the azimuthal separation of the particle and small perturbing body, and K , the Keplerian orbital energy of the particle about the central body.

The map captures well the dynamics of the full equations of motion; namely, the phase space is densely covered by chains of stable resonant islands, in between which is a connected chaotic zone. The chaotic zone, far from being structureless, contains lanes of fast migration between orbits of different semimajor axes. The advantage of having an analytical two-dimensional map over full numerical integration is that we can apply all the machinery of the theory of transport in symplectic twist maps [24, 19, 9].

An interesting consequence of the approximation used to construct the map is that the time-reversal symmetry of the original Hamiltonian system is broken, albeit slightly. The origins of this symmetry breaking and development of a modified approximation process to avoid it are currently under investigation.

Other authors have considered similar maps, so-called Keplerian maps, to study the long-time evolution of nearly parabolic comets and comet-like objects [6, 36, 21]. By including the dependence of the map on the Keplerian energy K , we have achieved

one of the goals of [16], which allows us to consider the map for orbits of moderate eccentricities and semimajor axes.

Our application is different from these papers. We apply our Keplerian map to the identification of transfer trajectories applicable to spacecraft transfers in a planet-moon system. The use of subtle gravitational effects described by the map may be feasible for future missions to explore the outer planet moon systems where the timescale of orbits is measured in days instead of years and low-energy trajectories may be considered for inter-moon transfers.

Physically, particles in the regime we study undergo multiple gravity assists of a different kind than the hyperbolic flybys of, say, the Voyager missions. The gravity assists we study are for particles on orbits with semimajor axes greater than the perturber's and whose periapsis passages occur close to, but beyond, the sphere of influence of the perturbing body (as conservatively estimated by the Hill sphere). The effect of gravity assists is largest for particles whose passages occur slightly behind (resp. in front of) the perturbing body, resulting in a larger (resp. smaller) semimajor axis. This makes the apoapsis distance grow (resp. shrink) while keeping the periapsis distance relatively unchanged.

Dramatic orbital changes result from repeated gravity assists which are timed such that changes accumulate steadily in one direction (e.g., steadily shrinking apoapsis distance). This process can be understood in terms of phase space transport between resonance zones, i.e., resonant gravity assist. It is a three-body problem phenomenon not amenable to a patched-conic approach. This work therefore fills a gap in the understanding of multiple gravity assist mission design, which has been successful for Jacobi constants (Tisserand parameters) much less than 3 where the subtle effects described here play little role [30].

This paper extends earlier work which considered the dynamical connection between resonances in the exterior realm and interior realm and their relationship to escape and capture from a planetary or satellite neighborhood [14]. With straightforward modifications, the method used here can be applied to orbits entirely in the interior realm, where the Poincaré map is taken at apoapsis (where the perturbation due to the small mass is greatest) instead of periapsis.

Future work will consider extension of the Keplerian map to include (i) out of plane motion, i.e., a four-dimensional symplectic map; (ii) multiple perturbers; (iii) eccentric orbits for the perturbers; and (iv) control and uncertainty [29]. This will increase the tools available to space mission designers and may shed light on the mechanism by which some minor bodies and impact ejecta get handed off between planets and moons of the solar system [11, 32, 13].

Given the success of the current application to celestial mechanics, we intend to investigate the general applicability of Picard's method of successive iterates to approximations of a Poincaré return map for perturbed Hamiltonian systems and other dynamical systems.

Acknowledgments. The authors thank Stefano Campagnola, Piyush Grover, Oliver Junge, Kartik Kumar, and Francois Lekien for interesting and insightful discussions, and anonymous referees for their helpful suggestions. S.D.R. acknowledges the support of National Science Foundation grant DMS 0402842.

REFERENCES

- [1] R. R. BATE, D. D. MUELLER, AND J. E. WHITE, *Fundamentals of Astrodynamics*, Dover, New York, 1971.
- [2] E. A. BELBRUNO AND J. K. MILLER, *Sun-perturbed Earth-to-Moon transfers with ballistic capture*, *Journal of Guidance, Control, and Dynamics*, 16 (1993), pp. 770–775.
- [3] G. D. BIRKHOFF, *Surface transformations and their dynamical applications*, *Acta Math.*, 43 (1920), pp. 1–119.
- [4] M. BRAUN, *Differential equations and their applications: an introduction to applied mathematics*, vol. 11 of *Texts in Applied Mathematics*, Springer-Verlag, New York, 4th ed., 1993.
- [5] D. BROUWER AND G. M. CLEMENCE, *Methods of Celestial Mechanics*, Academic Press, New York, 1961.
- [6] B. V. CHIRIKOV AND V. V. VECHESLAVOV, *Chaotic dynamics of comet Halley*, *Astronomy and Astrophysics*, 221 (1989), pp. 146–154.
- [7] C. C. CONLEY, *Low energy transit orbits in the restricted three-body problem*, *SIAM J. Appl. Math.*, 16 (1968), pp. 732–746.
- [8] ———, *Twist mappings, linking, analyticity, and periodic solutions which pass close to an unstable periodic solution*, in *Topological Dynamics*, J. Auslander, ed., New York, 1968, Benjamin, pp. 129–153.
- [9] M. DELLNITZ, O. JUNGE, W. S. KOON, F. LEKIEN, M. W. LO, J. E. MARSDEN, K. PADBERG, R. PREIS, S. D. ROSS, AND B. THIÈRE, *Transport in dynamical astronomy and multibody problems*, *Int. J. Bifurc. Chaos*, 15 (2005), pp. 699–727.
- [10] R. W. EASTON, J. D. MEISS, AND S. CARVER, *Exit times and transport for symplectic twist maps*, *Chaos*, 3 (1993), pp. 153–165.
- [11] B. J. GLADMAN, J. A. BURNS, M. DUNCAN, P. LEE, AND H. F. LEVISON, *The exchange of impact ejecta between terrestrial planets*, *Science*, 271 (1996), pp. 1387–1392.
- [12] G. GÓMEZ, W. S. KOON, M. W. LO, J. E. MARSDEN, J. MASDEMONT, AND S. D. ROSS, *Connecting orbits and invariant manifolds in the spatial three-body problem*, *Nonlinearity*, 17 (2004), pp. 1571–1606.
- [13] J. HORNER, N. W. EVANS, M. E. BAILEY, AND D. J. ASHER, *The populations of comet-like bodies in the Solar system*, *Mon. Not. R. Astron. Soc.*, 343 (2003), pp. 1057–1066.
- [14] W. S. KOON, M. W. LO, J. E. MARSDEN, AND S. D. ROSS, *Heteroclinic connections between periodic orbits and resonance transitions in celestial mechanics*, *Chaos*, 10 (2000), pp. 427–469.
- [15] ———, *Constructing a low energy transfer between Jovian moons*, *Contemporary Mathematics*, 292 (2002), pp. 129–145.
- [16] L. MALYSHKIN AND S. TREMAINE, *The Keplerian map for the planar restricted three-body problem as a model of comet evolution*, *Icarus*, 141 (1999), pp. 341–353.
- [17] J. E. MARSDEN AND S. D. ROSS, *New methods in celestial mechanics and mission design*, *Bulletin of the American Mathematical Society*, 43 (2006), pp. 43–73.
- [18] R. MCGEHEE, *Some homoclinic orbits for the restricted three-body problem*, PhD thesis, University of Wisconsin, Madison, 1969.
- [19] J. D. MEISS, *Symplectic maps, variational principles, and transport*, *Rev. Mod. Phys.*, 64 (1992), pp. 795–848.
- [20] J. MOSER, *Stable and Random Motions in Dynamical Systems with Special Emphasis on Celestial Mechanics*, Princeton University Press, 1973.
- [21] M. PAN AND R. SARI, *A generalization of the lagrangian points: Studies of resonance for highly eccentric orbits*, *Astronomical Journal*, 128 (2004), pp. 1418–1429.
- [22] M. E. PASKOWITZ AND D. J. SCHEERES, *Robust capture and transfer trajectories for planetary satellite orbiters*, *Journal of Guidance, Control, and Dynamics*, 29 (2006), pp. 342–353.
- [23] T. Y. PETROSKY AND R. BROUKE, *Area-preserving mappings and deterministic chaos for nearly parabolic motions*, *Celestial Mechanics*, (1988), pp. 53–79.
- [24] V. ROM-KEDAR AND S. WIGGINS, *Transport in two-dimensional maps*, *Arch. Rat. Mech. Anal.*, 109 (1990), pp. 239–298.
- [25] S. D. ROSS, W. S. KOON, M. W. LO, AND J. E. MARSDEN, *Design of a multi-moon orbiter*, in 13th AAS/AIAA Space Flight Mechanics Meeting, Ponce, Puerto Rico, February 2003. Paper No. AAS 03-143.
- [26] ———, *Application of dynamical systems theory to a very low energy transfer*, in 14th AAS/AIAA Space Flight Mechanics Meeting, Maui, Hawaii, February 2004. Paper No. AAS 04-289.
- [27] D. J. SCHEERES, *The effect of C_{22} on orbit energy and angular momentum*, *Celest. Mech. Dyn. Astron.*, 73 (1999), pp. 339–348.
- [28] ———, *Changes in rotational angular momentum due to gravitational interactions between two finite bodies*, *Celest. Mech. Dyn. Astron.*, 81 (2001), pp. 39–44.

- [29] D. J. SCHEERES, F.-Y. HSIAO, R. S. PARK, B. F. VILLAC AND J. M. MARUSKIN., *Fundamental Limits on Spacecraft Orbit Uncertainty and Distribution Propagation*, The Journal of the Astronautical Sciences (2007), to appear.
- [30] N. J. STRANGE AND J. M. LONGUSKI, *Graphical method for gravity-assist trajectory design*, Journal of Spacecraft and Rockets, 39 (2002), pp. 9–16.
- [31] V. SZEBEHELY, *Theory of Orbits: The Restricted Problem of Three Bodies*, Academic, New York, 1967.
- [32] M. TISCARENO AND R. MALHOTRA, *The dynamics of known Centaurs*, Astron. J., 126 (2003), pp. 3122–3131.
- [33] B. F. VILLAC, *Dynamics in the Hill problem with applications to spacecraft maneuvers*, PhD thesis, University of Michigan, 2003.
- [34] B. F. VILLAC AND D. J. SCHEERES, *On the concept of periapsis in Hill's problem*, Celestial Mechanics and Dynamical Astronomy, 90 (2004), pp. 165–178.
- [35] G. J. WHIFFEN, *An investigation of a Jupiter Galilean moon orbiter trajectory*, in AAS/AIAA Astrodynamics Specialist Conference, Big Sky, Montana, August 2003. Paper No. AAS 03-544.
- [36] J.-L. ZHOU, Y.-S. SUN, J.-Q. ZHENG, AND M. J. VALTONEN, *The transfer of comets from near-parabolic to short-period orbits: map approach*, Astronomy and Astrophysics, 364 (2000), pp. 887–893.